NONLINEAR UNMIXING OF VEGETATED AREAS: A MODEL COMPARISON BASED ON SIMULATED AND REAL HYPERSPECTRAL DATA

Nicolas Dobigeon[(1)], *Laurent Tits*[(2)], *Ben Somers*[(3)], *Yoann Altmann*[(1,4)] *and Pol Coppin*[(2)]

[(1)] University of Toulouse, IRIT/INP-ENSEEIHT/TéSA, Toulouse, France
[(2)] Department of Biosystems, KU Leuven, Belgium
[(3)] Division Forest, Nature and Landscape, KU Leuven, Belgium
[(4)] School of Engineering and Physical Sciences, Heriot-Watt University, Edinburgh, U.K.

ABSTRACT

When analyzing remote sensing hyperspectral images, numerous works dealing with spectral unmixing assume the pixels result from linear combinations of the endmember signatures. However, this assumption cannot be fulfilled, in particular when considering images acquired over vegetated areas. As a consequence, several nonlinear mixing models have been recently derived to take various nonlinear effects into account when unmixing hyperspectral data. Unfortunately, these models have been empirically proposed and without thorough validation. This paper attempts to fill this gap by taking advantage of two sets of real and physical-based simulated data. The accuracy of various linear and nonlinear models and the corresponding unmixing algorithms is evaluated with respect to their ability of fitting the sensed pixels and of providing accurate estimates of the abundances.

Index Terms— Hyperspectral imagery, spectral unmixing, nonlinear spectral mixtures, vegetated areas, ray tracing.

1. INTRODUCTION

For several decades, hyperspectral imaging has been an efficient tool widely used in spectroscopy, remote sensing and astrophysics. Thanks to their high spectral resolution, hyperspectral images can provide a discriminative mapping of the materials present in the sensed image. However, due to their inherent limited spatial resolution, recovering the spatial distribution of these materials over the observed scene usually requires to perform spectral unmixing (SU). Formally, SU consists of identifying the spectral responses $\mathbf{m}_1, \ldots, \mathbf{m}_R$ of the R macroscopic materials (or *endmembers*) present in the image and, for each pixel $\mathbf{y}_p$ ($p = 1, \ldots, P$), estimating the corresponding proportions $a_{1,p}, \ldots, a_{R,p}$ (or *abundances*) that represent the spatial coverage of these materials over the area of interest [1]. This problem has motivated an amount of research works in the remote sensing and image processing literatures, dedicated to the design of automated unmixing algorithms. The interested reader is invited to consult [1–3] for recent overviews of these unmixing methods. Most of these algorithms exploit intuitive geometrical concepts, that rely on the implicit assumption that the observed pixels result from linear combinations of the endmember spectra. According to this linear mixing model (LMM), each observed pixel spectrum of a given image can be expressed as

$$\mathbf{y}_p^{(\text{LMM})} = \sum_{r=1}^{R} a_{r,p}\mathbf{m}_r + \mathbf{n}_p = \mathbf{M}\mathbf{a}_p + \mathbf{n}_p \tag{1}$$

where $\mathbf{a}_p = [a_{1,p}, \ldots, a_{R,p}]^T$ denotes the proportions of the R materials in the pth pixel, $\mathbf{M} = [\mathbf{m}_1, \ldots, \mathbf{m}_R]$ is the endmember matrix and $\mathbf{n}_p$ stands for an additive residual term accounting for the measurement noise and modeling error. Since the mixing coefficients $a_{1,p}, \ldots, a_{R,p}$ are expected to represent the spatial distribution of the materials in the pth pixel, they are commonly subject to the following positivity and sum-to-one (or additivity) constraints

$$\begin{cases} a_{r,p} \geq 0, & \forall r,\ \forall p \\ \sum_{r=1}^{R} a_{r,p} = 1, & \forall p. \end{cases} \tag{2}$$

The LMM has been advocated in many applicative contexts since it can be considered as an admissible first-order approximation of the physical processes involved in image forming. Unfortunately, LMM has also demonstrated some limitations to accurately describe real mixtures in specific scenarios. Specifically, when the images are acquired over vegetated areas, more complex interactions (in particular multiple scattering effects) occur and they can not be properly handled by a simple LMM [4–6]. To overcome these difficulties, various nonlinear mixing models and associated unmixing techniques have been recently proposed [7]. In particular, when analyzing vegetated areas, most of these nonlinear models can be defined as

$$\mathbf{y}_p = \mathbf{M}\mathbf{a}_p + \boldsymbol{\mu}\left(\mathbf{M}, \mathbf{a}_p, \mathbf{b}_p\right) + \mathbf{n}_p. \tag{3}$$

In (3), the observed pixel is composed of a linear contribution similar to the LMM and an additive nonlinear term $\boldsymbol{\mu}(\cdot)$ that may depend on the endmember matrix $\mathbf{M}$, the abundance coefficients in $\mathbf{a}_p$ and additional nonlinearity coefficients $\mathbf{b}_p$ introduced to adjust the amount of nonlinearity in the pixel. This class of models includes the bilinear models [8], the quadratic-linear model [9], the post-nonlinear model [10] and the bilinear-bilinear model [11]. However, to the authors' knowledge, the accuracy and the ability of these models to properly describe real mixtures have never been carefully investigated. Indeed, such study requires to have available real or, at least, realistic hyperspectral data along with their ground truth, i.e., the spectral signatures of the endmembers and their actual abundances in each pixel of the scene. In this article, the authors take advantage of an interesting set of simulated and in-situ collected hyperspectral data to fill this gap and to evaluate the relevance of various nonlinear models.

This paper is organized as follows. The mixing models under consideration in this work are recalled in Section 2. The hyperspectral data used to validate these models are described in Section 3. The experiment results are reported in Section 4. Section 5 concludes the paper with a discussion on these results.

Part of this work has been supported by the Hypanema ANR Project no. ANR-12-BS03-003, the Direction Générale de l'Armement, French Ministry of Defence, the Research Foundation Flanders (FWO) project G.0677.13N, and the EPSRC via grant EP/J015180/1.

2. MIXING MODELS

The most popular existing nonlinear mixing models derived to describe vegetated areas mainly differ by the definition of the nonlinear component $\boldsymbol{\mu}(\mathbf{M}, \mathbf{a}_p, \mathbf{b}_p)$ in (3). In this study, four models are considered and introduced in what follows. In [5] and [12], nonlinearities are quantified by additional coefficients $\{b_{i,j,p}\}_{i,j}$ that are included within the set of constraints (2) defined by the LMM, leading to the so-called *Nascimento model* (NM)

$$\mathbf{y}_p^{(\text{NM})} \triangleq \sum_{r=1}^{R} a_{r,p}\mathbf{m}_r + \sum_{i=1}^{R-1}\sum_{j=i+1}^{R} b_{i,j,p}\mathbf{m}_i \odot \mathbf{m}_j + \mathbf{n}_p$$

with

$$\begin{cases} a_{r,p} \geq 0, \quad \forall r,\ \forall p \\ b_{i,j,p} \geq 0, \quad \forall r,\ \forall i \neq j \\ \sum_{r=1}^{R} a_{r,p} + \sum_{i=1}^{R-1}\sum_{j=i+1}^{R} b_{i,j,p} = 1, \ \ \forall p. \end{cases}$$

where the operator $\odot$ stands for a termwise product. When $b_{i,j,p} = 0, \forall i \neq j$, this model reduces to the LMM. However, the abundance coefficients $a_{1,p}, \ldots, a_{R,p}$ are not subject to the usual sum-to-one constraints defined in (2).

In [13], Fan *et al.* propose to relate the amount of nonlinear interactions to the amount of linear contribution (governed by $a_{r,p}$)

$$\mathbf{y}_p^{(\text{FM})} \triangleq \sum_{r=1}^{R} a_{r,p}\mathbf{m}_r + \sum_{i=1}^{R-1}\sum_{j=i+1}^{R} a_{i,p}a_{j,p}\mathbf{m}_i \odot \mathbf{m}_j + \mathbf{n}_p.$$

Under this so-called *Fan model* (FM), if a component $\mathbf{m}_i$ is absent in the pth pixel, then $a_{i,p} = 0$ and consequently there are no interactions between the material $\mathbf{m}_i$ and any other materials $\mathbf{m}_j$ ($j \neq i$). Note however that this bilinear model does not extend the LMM.

To cope with this later limitation, the generalized bilinear model (GBM) [14] adjusts the products of abundances $a_{i,p}a_{j,p}$ by additional free parameters $\gamma_{i,j,p} \in (0, 1)$ that tune the amount of nonlinear interactions, leading to

$$\mathbf{y}_p^{(\text{GBM})} \triangleq \sum_{r=1}^{R} a_{r,p}\mathbf{m}_r + \sum_{i=1}^{R-1}\sum_{j=i+1}^{R} \gamma_{i,j,p}a_{i,p}a_{j,p}\mathbf{m}_i \odot \mathbf{m}_j + \mathbf{n}_p.$$

The GBM has the nice properties of (*i*) generalizing the LMM by enforcing $\gamma_{i,j,p} = 0\ (\forall i, j)$, similarly to NM but contrary to FM and (*ii*) having the amount of nonlinear interactions to be proportional to the material abundances, similarly to FM but contrary to NM.

The fourth nonlinear model under consideration in this work has been introduced in [10] and relies on a second-order polynomial expansion of the nonlinearity, leading to the following polynomial post-nonlinear mixing model (PPNM)

$$\mathbf{y}_p^{(\text{PPNM})} = \mathbf{M}\mathbf{a}_p + b_p\left(\mathbf{M}\mathbf{a}_p\right) \odot \left(\mathbf{M}\mathbf{a}_p\right) + \mathbf{n}_p. \tag{4}$$

The PPNM has demonstrated a noticeable flexibility to model various nonlinearities not only for unmixing purposes [10] but also to detect nonlinear mixtures in the observed image [15].

3. DATA DESCRIPTION

The mixing models described in the previous section have been confronted with two sets of hyperspectral data representative of vegetated areas. These datasets are described below.

3.1. Simulated orchard scene

A synthetic but realistic fully calibrated virtual scene has been designed using methods developed in [16]. More precisely, two different orchard scenes have been generated: (*i*) an orchard consisting of citrus trees and a soil background, leading to two-endmember mixtures and (*ii*) an orchard consisting of citrus trees, a soil background and weed patches, leading to three-endmember mixtures. The orchards have been constructed with a row spacing of 4.0m, tree spacing of 2m, row azimuth of 7.3° and an average tree height of 3m. This composition is consistent with the reference orchard, located in Wellington, South Africa (33.58°S, 18.93°E), used to calibrate the virtual orchard [16]. Then, corresponding hyperspectral images have been simulated using an extended version of the physically based ray tracer (PBRT) [17]. Each orchard scene consists of 20×20 pixels, with a pixel resolution of 2m$\times$2m. The reference spectral signatures are known for the three components, as well as the exact per-pixel abundances. For a detailed description of this experiment, the reader is invited to consult [16].

3.2. Real orchard scene

The second dataset consists of a set of real hyperspectral spectra acquired over the same orchard used for the calibration of the virtual orchard described in paragraph 3.1. The inter-row spacing of the 3m tall trees was 4.5m and the inter-tree spacing 2.5m. In-situ measured reflectance spectra of 60 mixed ground plots have been collected throughout the orchard: 25 mixtures of tree and soil, 25 mixtures of tree and weed, and 25 mixtures of tree, soil and weed. The endmember spectra have been acquired by measuring pure soil and sunlit crown spectra in each scenario. Information on the ground cover composition of each of the measured mixed pixels has been extracted from digital photographs, as detailed in [5].

4. EXPERIMENTAL RESULTS

To evaluate the relevance of the models detailed in Section 2 with respect to the hyperspectral datasets described in Section 3, ground truth associated with the image pixels is exploited. More precisely, for both kinds of datasets, based on the prior knowledge of the actual pure component spectral signatures (i.e., endmember spectra), abundances are estimated according to the LMM, NM, FM and PPNM. The LMM-based abundances are estimated using the fully constrained least square (FCLS) algorithm [18]. Following the constraints in (2), the NM can be interpreted as a linear mixture of an extended set of endmembers, as shown in [12]. Thus, FCLS has been also used to unmix the pixels according to the NM. The FM parameters are estimated with the first-order Taylor expansion-based algorithm detailed in [13]. Finally, the gradient descent and the subgradient descend algorithms developed in [19] and [10] are used to solve the GBM- and PPNM-based unmixing problems, respectively.

Once the abundances (and possibly other nonlinearity parameters) have been estimated following the linear and nonlinear models, the relevance of these models is evaluated with respect to two figures-of-merit. First, we monitor their ability of accurately describing the physical processes yielding the considered mixtures by computing the average square reconstruction error (RE)

$$\text{RE} = \frac{1}{LP}\sum_{p=1}^{P} \|\mathbf{y}_p - \hat{\mathbf{y}}_p\|^2 \tag{5}$$

where $\|\cdot\|$ stands for the usual Euclidean norm ($\|\mathbf{x}\| = \sqrt{\mathbf{x}^T\mathbf{x}}$). In the right-hand side of (5), $\mathbf{y}_p$ ($p = 1, \ldots, P$) are the observed pixels whereas $\hat{\mathbf{y}}_p$ are the corresponding estimates given by $\hat{\mathbf{y}}_p = \mathbf{M}\hat{\mathbf{a}}_p + \boldsymbol{\mu}\left(\mathbf{M}, \hat{\mathbf{a}}_p, \hat{\mathbf{b}}_p\right)$ where $\boldsymbol{\mu}(\cdot)$ is equal to 0 for the LMM or stands for the additional nonlinear contribution for the nonlinear models. Secondly, the mean reconstruction difference in the ℓth band, is considered to visualize the influence of wavelengths,

$$\mathrm{RD}_\ell = \frac{1}{P}\sum_{p=1}^{P}(y_{\ell,p} - \hat{y}_{\ell,p})\,.$$

Finally, we evaluate the ability of the considered models for providing meaningful estimations of the abundance coefficients by computing the mean square errors (MSE) between the actual abundance vectors $\mathbf{a}_p$ and the corresponding estimated $\hat{\mathbf{a}}_p$ $(p = 1, \ldots, P)$

$$\mathrm{MSE} = \frac{1}{RP}\sum_{p=1}^{P}\|\mathbf{a}_p - \hat{\mathbf{a}}_p\|^2\,.$$

4.1. Simulated orchard dataset

The unmixing results for the simulated orchard scenes are shown in Table 1 in terms of MSE and RE. From these results, for both two- and three-endmembers, one can conclude that NM and LMM perform similarly in term of RE, while PPNM and FM provide the best results and, in particular, significantly better than LMM. Regarding the abundance MSE, NM and LMM provide similar errors for two-endmember mixtures and all nonlinear models perform better than LMM for three-endmember mixtures. In Fig. 1, the RDs are depicted as functions of wavelength, for the different linear and nonlinear mixing models.

	RE		MSE	
	2 endm.	3 endm.	2 endm.	3 endm.
LMM	7.70	5.81	**0.96**	3.17
FM	**1.24**	**0.91**	1.13	**2.27**
NM	7.70	5.81	**0.92**	**2.44**
GBM	10.13	0.94	1.47	2.45
PPNM	**1.28**	**0.91**	1.22	2.62

Table 1: Two- and three-endmember orchard synthetic dataset. Abundance MSE ($\times 10^{-2}$) and RE ($\times 10^{-4}$) for various linear/nonlinear mixing models.

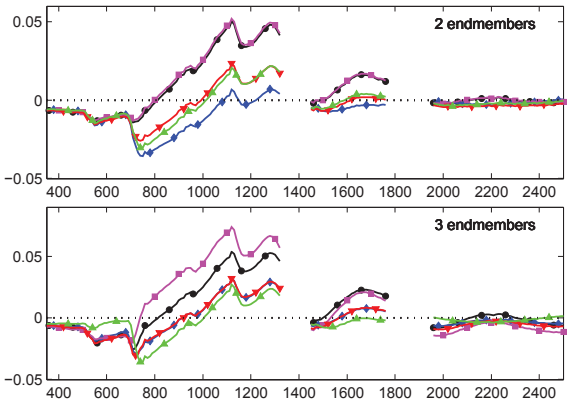

Fig. 1: Two- and three-endmember orchard synthetic dataset. Reconstruction difference RD_ℓ as a function of wavelength for various linear/nonlinear mixing models: LMM (black), FM (blue), NM (magenta), GBM (red) and PPNM (green).

4.2. In-situ orchard measurements

Table 2 reports the reconstruction error of the mixed signal and the accuracy of the estimated abundances. Once again, PPNM is the mixing model that reconstructs the mixed signatures the best, while FM performed worse than the LMM. For the abundance accuracy, MSE results are less homogeneous than those obtained with the various simulated datasets. Depending on the type of the mixture, GBM or PPNM are the best unmixing model, while FM gives the lowest abundance estimation accuracies. The RDs obtained on the in-situ measurements are depicted in Fig. 2. From these plots, most of the mixing models seem to be not sufficiently accurate to capture the nonlinearities in the observed mixtures, except the PPNM.

		tree-weed	tree-soil	tree-soil-weed
RE	LMM	16.4	27.1	6.80
	FM	17.7	16.4	10.9
	NM	16.3	26.8	2.13
	GBM	15.9	15.2	6.71
	PPNM	**3.07**	**1.82**	**1.21**
MSE	LMM	**12.5**	2.78	6.42
	FM	13.5	2.88	8.15
	NM	12.6	**2.71**	**5.80**
	GBM	**12.2**	2.86	6.39
	PPNM	13.0	**2.57**	**4.83**

Table 2: Two- and three-endmember in-situ measurements. Abundance MSE ($\times 10^{-2}$) and RE ($\times 10^{-4}$) for various linear/nonlinear mixing models.

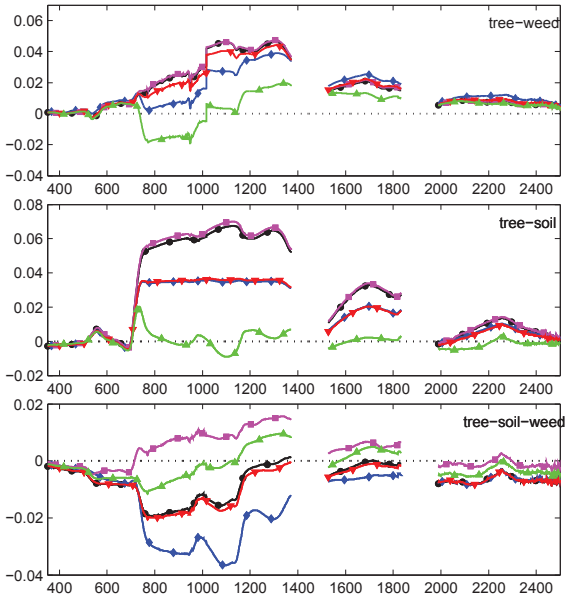

Fig. 2: Two- and three-endmember in-situ measurements. Reconstruction difference RD_ℓ as a function of wavelength for various linear/nonlinear mixing models: LMM (black), FM (blue), NM (magenta), GBM (red) and PPNM (green).

5. CONCLUDING REMARKS

The results reported in Section 4 show that a better modeling of the mixed pixels (i.e., with low RE) does not necessarily result in a better estimation of the abundances (i.e., with low MSE). For instance, PPNM, which has been shown to be very accurate to model nonlinearties in most cases, sometimes lead to less accuracy with respect to

the abundance estimation when compared to LMM, in particular for the two-endmember mixtures in the simulated (see Table 1) and for the tree-weed mixtures in the in-situ data (see Table 2). This demonstrates that the model fitting error, widely used in the remote sensing literature to monitor the performance of the unmixing algorithm, can not be used as the unique figure-of-merit to evaluate the relevance of a given mixing model.

Moreover, all nonlinear mixing models considered in Section 2 implicitly assume the same amount of nonlinearity for each wavelength of the spectral domain. However, from the RDs depicted in Fig.'s 1 and 2, it clearly appears that the mis-modeling is drastically subjected to the influence of the wavelength. This corroborates the results of Somers *et al.* who also noticed similar behavior for the bilinear mixing model [6].

It is also worth noting that unmixing algorithms have been used to estimate the parameters involved in the model specification (e.g., abundances and nonlinearity parameters). Unfortunately, the optimization problems to be solved to recover the abundance coefficients are not totally straightforward, mainly due to the constraints and/or the nonlinearity. As a consequence, the reliability of the obtained results, in terms of RE and abundance MSE, should be carefully analyzed, indeed mitigated. More precisely, part of the REs may consist of approximation errors induced by the unmixing algorithms themselves. As an archetypal example, results in Table 1 show that the GBM provides worse results than LMM and FM for the two-endmember mixtures although GBM is supposed to generalize the two other models.

Finally, the authors would like to mention that complementary results, in particular obtained on another dataset, are reported in the companion paper [20] and that the data used in this study will be available online[1].

6. REFERENCES

[1] N. Keshava and J. F. Mustard, "Spectral unmixing," *IEEE Signal Process. Mag.*, vol. 19, no. 1, pp. 44–57, Jan. 2002.

[2] B. Somers, G. P. Asner, and L. Tits, "Endmember variability in spectral: a review," *Remote Sens. Environment*, vol. 115, no. 7, pp. 1603–1616, July 2011.

[3] J. M. Bioucas-Dias, A. Plaza, N. Dobigeon, M. Parente, Q. Du, P. Gader, and J. Chanussot, "Hyperspectral unmixing overview: Geometrical, statistical, and sparse regression-based approaches," *IEEE J. Sel. Topics Appl. Earth Observations and Remote Sens.*, vol. 5, no. 2, pp. 354–379, April 2012.

[4] L. Tits, W. Delabastita, B. Somers, J. Farifteh, and P. Coppin, "First results of quantifying nonlinear mixing effects in heterogeneous forests: A modeling approach," in *Proc. IEEE Int. Conf. Geosci. Remote Sens. (IGARSS)*, 2012, pp. 7185–7188.

[5] B. Somers, K. Cools, S. Delalieux, J. Stuckens, D. V. der Zande, W. W. Verstraeten, and P. Coppin, "Nonlinear hyperspectral mixture analysis for tree cover estimates in orchards," *Remote Sens. Environment*, vol. 113, pp. 1183–1193, Feb. 2009.

[6] B. Somers, L. Tits, and P. Coppin, "Quantifying nonlinear spectral mixing in vegetated areas: computer simulation model validation and first results," *IEEE J. Sel. Topics Appl. Earth Observations and Remote Sens.*, 2014, to appear.

[1] http://www.biw.kuleuven.be/nonlinear-mixing/

[7] N. Dobigeon, J.-Y. Tourneret, C. Richard, J. C. M. Bermudez, S. McLaughlin, and A. O. Hero, "Nonlinear unmixing of hyperspectral images: Models and algorithms," *IEEE Signal Process. Mag.*, vol. 31, no. 1, pp. 89–94, Jan. 2014.

[8] Y. Altmann, N. Dobigeon, and J.-Y. Tourneret, "Bilinear models for nonlinear unmixing of hyperspectral images," in *Proc. IEEE GRSS Workshop Hyperspectral Image SIgnal Process.: Evolution in Remote Sens. (WHISPERS)*, Lisbon, Portugal, June 2011, pp. 1–4.

[9] I. Meganem, P. Déliot, X. Briottet, Y. Deville, and S. Hosseini, "Linear-quadratic mixing model for reflectances in urban environments," *IEEE Trans. Geosci. and Remote Sens.*, vol. 52, no. 1, pp. 544–558, Jan. 2014.

[10] Y. Altmann, A. Halimi, N. Dobigeon, and J.-Y. Tourneret, "Supervised nonlinear spectral unmixing using a post-nonlinear mixing model for hyperspectral imagery," *IEEE Trans. Image Process.*, vol. 21, no. 6, pp. 3017–3025, June 2012.

[11] O. Eches and M. Guillaume, "A bilinear-bilinear non-negative matrix factorization method for hyperspectral unmixing," *IEEE Geosci. and Remote Sens. Lett.*, vol. 11, no. 4, pp. 778–782, April 2014.

[12] J. M. P. Nascimento and J. M. Bioucas-Dias, "Nonlinear mixture model for hyperspectral unmixing," in *Proc. SPIE Image and Signal Processing for Remote Sensing XV*, L. Bruzzone, C. Notarnicola, and F. Posa, Eds., vol. 7477, no. 1. SPIE, 2009, p. 74770I.

[13] W. Fan, B. Hu, J. Miller, and M. Li, "Comparative study between a new nonlinear model and common linear model for analysing laboratory simulated-forest hyperspectral data," *IJRS*, vol. 30, no. 11, pp. 2951–2962, June 2009.

[14] A. Halimi, Y. Altmann, N. Dobigeon, and J.-Y. Tourneret, "Nonlinear unmixing of hyperspectral images using a generalized bilinear model," *IEEE Trans. Geosci. and Remote Sens.*, vol. 49, no. 11, pp. 4153–4162, Nov. 2011.

[15] Y. Altmann, N. Dobigeon, and J.-Y. Tourneret, "Nonlinearity detection in hyperspectral images using a polynomial post-nonlinear mixing model," *IEEE Trans. Image Process.*, vol. 22, no. 4, pp. 1267–1276, April 2013.

[16] J. Stuckens, B. Somers, S. Delalieux, W. W. W. Verstraeten, and P. Coppin, "The impact of common assumptions on canopy radiative transfer simulations: a case study in citrus orchards," *J. Quantitative Spectroscopy and Radiative Transfer*, vol. 110, no. 1–2, pp. 1–21, Jan. 2009.

[17] M. Pharr and G. Humphreys, *Physically Based Rendering: From Theory to Implementation*, T. Cox, Ed. San Fransisco: Morgan Kaufmann Pub, 2004.

[18] D. C. Heinz and C. -I Chang, "Fully constrained least-squares linear spectral mixture analysis method for material quantification in hyperspectral imagery," *IEEE Trans. Geosci. and Remote Sens.*, vol. 29, no. 3, pp. 529–545, March 2001.

[19] A. Halimi, Y. Altmann, N. Dobigeon, and J.-Y. Tourneret, "Unmixing hyperspectral images using the generalized bilinear model," in *Proc. IEEE Int. Conf. Geosci. Remote Sens. (IGARSS)*, Vancouver, Canada, July 2011, pp. 1886–1889.

[20] N. Dobigeon, L. Tits, B. Somers, Y. Altmann, and P. Coppin, "A comparison of nonlinear mixing models for vegetated areas using simulated and real hyperspectral data," *IEEE J. Sel. Topics Appl. Earth Observations and Remote Sens.*, 2014, submitted. [Online]. Available: http://arxiv.org/abs/1312.1270/